

Article

Dispersion and Stabilization of Supported Layered Double Hydroxide-Based Nanocomposites on V-Based Catalysts for Nonoxidative Dehydrogenation of Isobutane to Isobutene

Fanji Liu ¹, Mingxun Han ¹, Xiangxiang Li ¹, Xiqing Zhang ¹, Yanting Wang ¹, Yanhong Xu ² and Lihong Zhang ^{1,*} 

¹ Department of Catalysis Science and Technology and Tianjin Key Laboratory of Applied Catalysis Science & Technology, School of Chemical Engineering and Technology, Tianjin University, Tianjin 300350, China; lfj19961018@163.com (F.L.); hanmingxun0401@163.com (M.H.); lixx_37@tju.edu.cn (X.L.); zhangxiqing1997@163.com (X.Z.); w2016016061@163.com (Y.W.)

² School of Chemical & Environmental Engineering, Pingdingshan University, Pingdingshan 467000, China; joanxu-2001@sohu.com

* Correspondence: zlh_224@tju.edu.cn; Tel.: +86-150-2225-5828

Abstract: Nonoxidative dehydrogenation of isobutane is one of the sustainable strategies for producing high value added isobutene. As alternatives for the commercial Pt- and Cr-based dehydrogenation catalysts, supported V-based catalysts are worthy of study. In this work, a series of VO_x/mMgAlO-R catalysts (m = 10, 15, 20, 25 and 30) were designed and prepared by loading VO_x on mMgAlO composite oxide supports derived from mesoporous Al₂O₃-supported layered double hydroxide (LDH) nanocomposites. The calcined and reduced catalysts were characterized by X-ray diffraction (XRD), Raman spectra, Ultraviolet-visible diffuse reflectance (UV-Vis) spectra, NH₃ temperature-programmed desorption (NH₃-TPD), Temperature-programmed reduction (H₂-TPR), X-ray photoelectron spectroscopy (XPS), thermogravimetric analysis (TG) and low temperature N₂ adsorption-desorption isotherms. The as-synthesized VO_x/20MgAlO-R with appropriate Mg addition exhibits superior activity (43–56% conversion and 77–81% selectivity), excellent stability and coking-resistance for the isobutane dehydrogenation. The structure-performance relationship reveals that the formation of VO_x species confined in the reconstructed LDH interlayer and porous MgO facilitates dispersing and stabilizing the VO_x species. The low polymerization degree and higher proportion of V⁴⁺ ion for VO_x species, strong acidity of medium acid sites and low concentration of strong acid sites are responsible for the excellent anti-coking and catalytic performance. The strong VO_x-support interaction is beneficial for enhancing the stability of the catalysts.

Keywords: isobutane dehydrogenation; layered double hydroxide; vanadium-based catalysts; magnesium modification; polymerization degree



Citation: Liu, F.; Han, M.; Li, X.; Zhang, X.; Wang, Y.; Xu, Y.; Zhang, L. Dispersion and Stabilization of Supported Layered Double Hydroxide-Based Nanocomposites on V-Based Catalysts for Nonoxidative Dehydrogenation of Isobutane to Isobutene. *Catalysts* **2022**, *12*, 382. <https://doi.org/10.3390/catal12040382>

Academic Editor: Maria Luisa Di Gioia

Received: 8 March 2022

Accepted: 28 March 2022

Published: 29 March 2022

Publisher's Note: MDPI stays neutral with regard to jurisdictional claims in published maps and institutional affiliations.



Copyright: © 2022 by the authors. Licensee MDPI, Basel, Switzerland. This article is an open access article distributed under the terms and conditions of the Creative Commons Attribution (CC BY) license (<https://creativecommons.org/licenses/by/4.0/>).

1. Introduction

Isobutene is an important raw material to produce highly valued chemicals, such as methyl-tert-butyl ether, methacrylate polymers, butyl rubber and polyisobutylene [1]. In recent years, the demand for isobutene has been rapidly growing worldwide, and its production process has received more and more attention [2]. Compared with nonoxidative dehydrogenation, the reactants and products are further oxidized even in the presence of a small amount of O₂ due to the strong oxidizing properties of O₂ during oxidative dehydrogenation, thus reducing the selectivity of the products [3]. The nonoxidative dehydrogenation of isobutane is one of the significant ways to produce isobutene. For the process, the most important work is to develop an efficient and stable catalyst [1,4,5]. Although Pt- and CrO_x-based catalysts have been widely used in industry, the high cost and toxicity of Pt- and CrO_x-based catalysts has prompted some scientists to focus their work on the less costly and less hazardous non-noble metal oxide catalysts, such as VO_x, GaO_x, ZnO and FeO_x [3,6–12].

The high dehydrogenation performance and regeneration stability have made VO_x -based catalysts one of the important alternative non-noble metal oxide catalysts widely used in oxidative dehydrogenation [13–15] and nonoxidative dehydrogenation of alkanes [3,10,11]. Usually, the catalytic performance and coking behavior are closely related to the surface acid–base properties and chemical state of VO_x species. As for the valence states of VO_x species, it is usually accepted that V^{3+} , V^{4+} and V^{5+} ions could appear together, but only V^{3+} and V^{4+} ions are often considered as the active species [10,16–18]. Some reports have emphasized that only the isolated V^{3+} and V^{4+} could be identified as dehydrogenation active sites [19,20]. Certainly, the single V^{3+} ion was also found to be more active for dehydrogenation under certain conditions [21,22]. On the other hand, the polymerization degree (namely aggregation degree) of VO_x also plays an important role in promoting dehydrogenation and resisting coke formation [10,17,20,23]. Generally, the isolated and low polymerized VO_x are more active than the aggregated V_2O_5 [24,25]. However, the aggregated VO_x species have also been reported to perform better than isolated VO_x species [11]. Therefore, it is still necessary to investigate the structure–performance relationship of the VO_x -based catalysts under different conditions.

As a commonly used support, Al_2O_3 has been extensively studied in the dehydrogenation process due to the high specific surface area, excellent thermal stability and adjustable physical and chemical properties [11,25–27]. Undoubtedly, the phase structure of Al_2O_3 could influence the surface acidity, structure and dispersion of VO_x species [26,27]. The slight difference in the surface VO_x species dispersion depends on the different density of surface hydroxyl groups on $\gamma\text{-Al}_2\text{O}_3$ and $\delta\text{-Al}_2\text{O}_3$ [27], while the crystallization temperature of Al_2O_3 also can influence the proportion of polymerized VO_x species and V^{4+} state, which is associated with the surface acid sites [11]. The use of alkaline promoters is another way to modify the dehydrogenation performance of catalysts [13–15]. The addition of Mg can not only change the distribution and strength of surface acid sites, but also improve the stability and dispersion of VO_x species [25]. The alkaline earth hydroxyapatite-supported V_2O_5 displayed good dispersity and high selectivity to the desired product in the oxidative dehydrogenation of alkane [13–15]. Recently, there have been reports on catalysts made of combined V, Mg and Al in the nonoxidative dehydrogenation of alkane [25]. Besides Al_2O_3 , the layered double hydroxide (LDH)-derived MgAlO composite oxide is also regarded as an excellent support applied in dehydrogenation reaction, because of its appropriate acid–base properties, easy reconstruction due to the memory effect and atomic-scale uniform distribution of metal species arising from the topotactic transformation [28–31]. However, most reports focus on the LDH derivative-supported Pt-based catalysts, while the studies on LDH-derived VO_x -based catalysts are seldomly reported in the dehydrogenation reaction.

In this study, the in situ grown MgAl-LDH derivatives on the surface of Al_2O_3 were prepared as composite supports to disperse and stabilize VO_x species by reconstructing a brucite-like structure and forming porous MgO. The physicochemical properties of these catalysts and precursors were investigated by various methods, and the catalytic activity was evaluated in non-oxidative dehydrogenation of isobutane to isobutene. The target of this study is to investigate the effect of supported MgAl-LDH derivatives on the chemical states of VO_x species, surface acid–base properties, coking behavior and catalytic performance by changing the Mg content.

2. Results and Discussion

2.1. Characterization of Composite Oxide Supports and Catalysts

2.1.1. Phase Composition and Textural Characteristics of Catalysts

To confirm the phase structure of support precursors $m\text{MgAlO-P}$ ($m = 10, 15, 20, 25$ and 30), composite supports $m\text{MgAlO}$, supported catalysts $\text{VO}_x/m\text{MgAlO}$ and the corresponding precursors $\text{VO}_x/m\text{MgAlO-P}$, their X-ray diffraction (XRD) patterns are presented (see Figure 1). In Figure 1a, the strong characteristic diffraction peaks of the LDH phase can be detected at 2θ of ca. 11.7° , 23.6° , 34.9° , 39.6° , 47.1° , 60.9° and 62.2° for all $m\text{MgAlO-P}$ samples, which can be attributed to the diffraction peaks of the (003),

(006), (012), (015), (018), (110) and (113) planes of the LDH phase (JCPDS file No. 89-0640), respectively. There are no diffraction peaks of other phases, except the LDH phase can be recognized. This indicates the single LDH can be in situ formed on γ - Al_2O_3 .

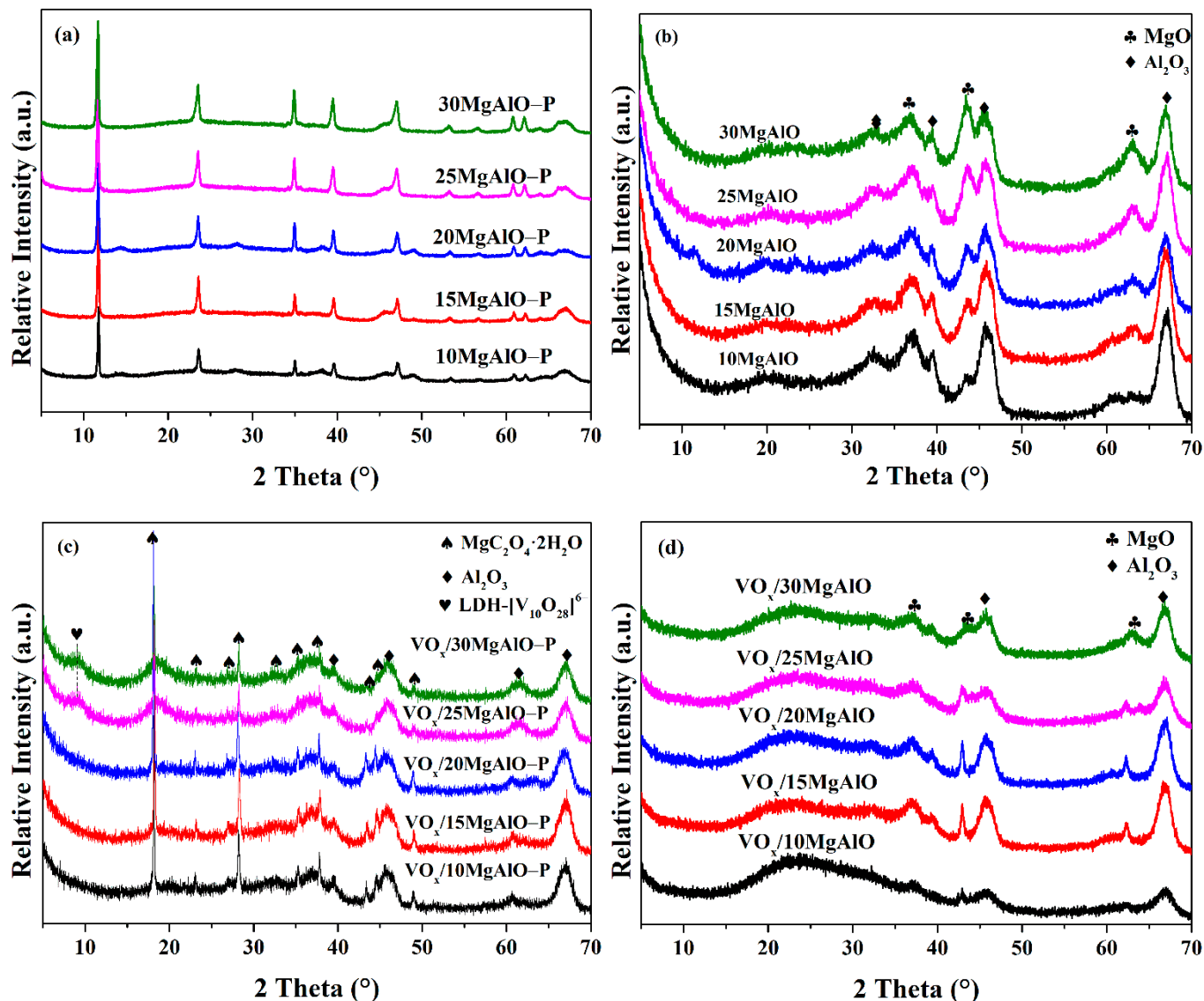


Figure 1. X-ray diffraction (XRD) patterns of samples at different stages: (a) mMgAlO-P, (b) mMgAlO, (c) $\text{VO}_x/\text{mMgAlO-P}$ and (d) $\text{VO}_x/\text{mMgAlO}$ ($m = 10, 15, 20, 25$ and 30).

After calcination, all diffraction peaks of the LDH phase disappear for the composite supports mMgAlO (see Figure 1b) due to the layered structure collapse of the LDH phase. Consequently, the characteristic diffraction peaks of the MgO phase (JCPDS file No. 45-0946) can be found at 2θ of ca. 42.9° and 62.3° , indexed as (200) and (220) planes, respectively, in addition to the diffraction peaks of γ - Al_2O_3 (JCPDS file No. 50-0741). In addition, the diffraction peak intensities of MgO have an obvious increase for 25MgAlO and 30MgAlO, with high Mg content, which means the excessive Mg addition can result in the growth of MgO crystallite size, even covering the partial VO_x species.

As shown in Figure 1c, the strong diffraction peaks of $\text{MgC}_2\text{O}_4 \cdot 2\text{H}_2\text{O}$ (glushinskite, JCPDS file No. 28-0625) can be found at 2θ of ca. 18.1° , 23.0° , 26.8° , 28.1° , 35.1° , 37.7° , 43.2° , 44.4° and 48.8° . The formation of the $\text{MgC}_2\text{O}_4 \cdot 2\text{H}_2\text{O}$ phase is related to the impregnation of mMgAlO with aqueous $(\text{NH}_4)_2[(\text{VO})_2(\text{C}_2\text{O}_4)_3]$ [32,33], which is the reaction product between NH_4VO_3 and oxalic acid. The acid environment makes the partial Mg^{2+}

cations dissolve from mMgAlO and react with the $(C_2O_4)^{2-}$ anion released from the $(NH_4)_2[(VO)_2(C_2O_4)_3]$ complex. By increasing the Mg loading from 10% to 30%, the diffraction peak intensities of $MgC_2O_4 \cdot 2H_2O$ show a slight increase and then decline sharply. The strongest diffraction of $MgC_2O_4 \cdot 2H_2O$ is obtained by $VO_x/20MgAlO-P$. This means there is a large amount of $MgC_2O_4 \cdot 2H_2O$ formed on $VO_x/20MgAlO-P$, which will result in many porous MgO formations by decomposing $MgC_2O_4 \cdot 2H_2O$ at high temperature [34]. This can be confirmed by the results of Figure 1d, Figure S1 (Supplementary Materials) and Table 1 below. In addition, no diffraction peaks can be attributed to VO_x species, but a weak diffraction peak can be found at 2θ of ca. 9.6° for $VO_x/25MgAlO-P$ and $VO_x/30MgAlO-P$. This can be mainly assigned to the decavanadate $[V_{10}O_{28}]^{6-}$ intercalated LDH phase (LDH- $[V_{10}O_{28}]^{6-}$) [34]. This indicates that the calcined LDH structure has a different chance to be reconstructed along with the formation of $MgC_2O_4 \cdot 2H_2O$, which depends on Mg content. In other words, the VO_x species can be introduced into the interlayer of the reconstructed LDH for all samples, although there is no obvious diffraction of LDH- $[V_{10}O_{28}]^{6-}$ in the XRD patterns for $VO_x/10MgAlO-P$, $VO_x/15MgAlO-P$ and $VO_x/20MgAlO-P$, which is owing to the poor crystallinity arising from low Mg content.

Table 1. Textural properties of the $VO_x/mMgAlO$ ($m = 10, 15, 20, 25$ and 30) catalysts.

Sample	S_{BET} ($m^2 \cdot g^{-1}$)	V_T ($cm^3 \cdot g^{-1}$)	D_{AP} (nm)	D_P (%)		
				2.5–7.5 nm	7.5–17.0 nm	17.0–30.0 nm
$VO_x/10MgAlO$	102	0.31	12.1	14.9	51.8	33.3
$VO_x/15MgAlO$	123	0.38	12.1	11.7	52.3	36.0
$VO_x/20MgAlO$	161	0.48	9.6	5.2	62.2	32.6
$VO_x/25MgAlO$	140	0.51	9.6	5.2	56.2	38.7
$VO_x/30MgAlO$	87	0.23	12.4	21.2	50.0	28.8

As expected, the diffraction peaks of $MgC_2O_4 \cdot 2H_2O$ disappear completely for $VO_x/mMgAlO$; instead, the diffraction peaks of MgO and $\gamma-Al_2O_3$ nanoparticles appear again (see Figure 1d). The variation trend of MgO diffraction peaks with Mg content is consistent with that of the $MgC_2O_4 \cdot 2H_2O$ precursor and different from that of initial MgO formed on mMgAlO supports (Figure 1b). This further indicates that the formation of $MgC_2O_4 \cdot 2H_2O$ can influence the MgO texture, as discussed above. Another important phenomenon is that diffraction peaks of VO_x species still cannot be detected for all samples of $VO_x/mMgAlO$, which are calcined $VO_x/mMgAlO-P$; this is related to the high dispersion of VO_x species, and the possibility of low V loading amount can be excluded in this work. In fact, the formation of lattice-confined VO_x species and porous MgO is beneficial for dispersing and stabilizing the VO_x species on the surface of mMgAlO [35].

Considering the possible influence of $MgC_2O_4 \cdot 2H_2O$ formation on the texture, the low temperature N_2 adsorption–desorption isotherms and pore size distribution (PSD) curves of fresh catalysts $VO_x/mMgAlO$ with different Mg content are given in Figure S1; the corresponding BET special surface area (S_{BET}), total pore volume (V_T), average pore size (D_{AP}) and pore size distribution percentage in different range (D_P) are listed in Table 1. As shown in Figure S1a, all catalysts show the typical type IV isotherms with H3 hysteresis loops. This indicates that all catalysts possess the typical slit-shaped mesoporous feature related to a layered structure [29,36], which arises from the topological transformation of the LDH structure [29]. The pore size distribution curves in Figure S1b also confirm the mesoporous feature of all catalysts.

From Table 1, it can be seen that the S_{BET} values increase from 102 to 161 $m^2 \cdot g^{-1}$, with the Mg content increasing from 10 to 20%, and then significantly decrease when the Mg content further increases. It is obvious that $VO_x/20MgAlO$ possesses the largest S_{BET} value of 161 $m^2 \cdot g^{-1}$ among all catalysts. At the same time, the continuous introduction of Mg has no influence on the V_T value of catalysts; on the contrary, it enhances this value from 0.31 $m^3 \cdot g^{-1}$ of $VO_x/10MgAlO$ to 0.51 $m^3 \cdot g^{-1}$ of $VO_x/25MgAlO$, except for

the lowest V_T value of $0.23 \text{ m}^3 \cdot \text{g}^{-1}$ for $\text{VO}_x/30\text{MgAlO}$. As seen in the D_P values in the range of 7.5–17.0 nm, they display a similar trend to that of the S_{BET} values, changing with Mg content. These results suggest that the $\text{VO}_x/\text{mMgAlO-P}$ precursors with more $\text{MgC}_2\text{O}_4 \cdot 2\text{H}_2\text{O}$ microcrystals enable more porous MgO formation, with higher S_{BET} and D_P values in the middle size range. This results agrees rather well with those discussed for XRD patterns above.

2.1.2. Polymerization Degree of VO_x Species

To analyze surface VO_x species, the catalysts $\text{VO}_x/\text{mMgAlO}$ with different Mg content were analyzed by Raman spectroscopy. As shown in Figure 2, no sharp characteristic Raman band can be found at 998 cm^{-1} for all catalysts, indicating that no V_2O_5 crystal particles are formed on the surface of these catalysts [11,27]. The results are consistent with those of XRD patterns above and ultraviolet-visible diffuse reflectance (UV-Vis) spectra below. It is worth mentioning that only sample $\text{VO}_x/20\text{MgAlO}$ exhibits a stronger band at 1070 cm^{-1} , which is attributed to the V=O bond stretching mode, suggesting the presence of more isolated tetrahedral-coordinated VO_x species on the surface of $\text{VO}_x/20\text{MgAlO}$ [11]. All samples display a weak signal at 488 cm^{-1} and a broad band in the range of $700\text{--}1000 \text{ cm}^{-1}$, which are caused by V-O-V and/or V-O-Al antisymmetric and symmetric stretching vibrations [3,10,11]. The appearance of these bands indicates the presence of polymerized VO_x species on the surface of catalysts. With the increase of Mg content, the broad band shifts from 941 to 895 cm^{-1} , and the red shift of this band indicates that the polymerization degree of VO_x species decreases [17]. We can also observe a doublet peak for $\text{VO}_x/30\text{MgAlO}$; the peak at 872 cm^{-1} is related to the existence of microcrystal $\text{Mg}_2\text{V}_2\text{O}_7$ [37,38]. At the same time, this broad band grows in intensity significantly from $\text{VO}_x/10\text{MgAlO}$ to $\text{VO}_x/15\text{MgAlO}$ and $\text{VO}_x/20\text{MgAlO}$, and then weakens obviously for $\text{VO}_x/25\text{MgAlO}$ and $\text{VO}_x/30\text{MgAlO}$, which reflects the quantity change of surface polymerized VO_x species. These differences indicate that the formation of moderate lattice-confined VO_x species and abundant porous MgO facilitates dispersing the VO_x species on the surface of mMgAlO [35,39].

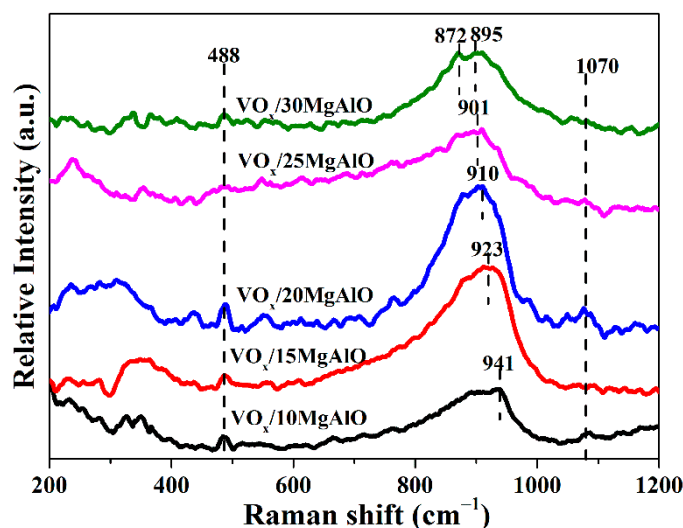


Figure 2. Raman spectra of the calcined catalyst $\text{VO}_x/\text{mMgAlO}$ ($m = 10, 15, 20, 25$ and 30).

All the catalysts $\text{VO}_x/\text{mMgAlO}$ are also characterized by the UV-Vis spectra to further determine the dispersion state of VO_x species on the composite supports mMgAlO, and the corresponding spectra are displayed in Figure 3. As shown in Figure 3a, an intense and broad UV-Vis adsorption band related to the $\text{O}^{2-} \rightarrow \text{V}^{5+}$ ligand to metal charge transfer (LMCT) can be found at ca. 275 nm, with a shoulder on the higher wavelength side for all samples. This means that the surface VO_x species are dominated by highly dispersed isolated VO_x species and low-polymerized VO_x species with tetrahedral coordination [10,11,40]. The weak absorption bands at 350–400 nm indicate that there are few

high-polymerized tetrahedral and distorted octahedral coordinated VO_x species on the surface of the catalysts [11]. In this region, a slight decrease in intensity can be found from $\text{VO}_x/10\text{MgAlO}$ and $\text{VO}_x/15\text{MgAlO}$ to others with high Mg content. It can be deduced that there are more isolated and low-polymerized VO_x species formed on $\text{VO}_x/20\text{MgAlO}$ than that on $\text{VO}_x/15\text{MgAlO}$. Furthermore, the absent bands between 400 and 600 nm indicate that there are no V_2O_5 crystals formed on the surface of catalysts [11], which is consistent with the results of XRD and Raman. The band at 208 nm is associated with $\text{O}^{2-} \rightarrow \text{V}^{4+}$ LMCT [41], and the absorption band increases slightly with the increase of Mg, indicating that more V^{4+} species are formed.

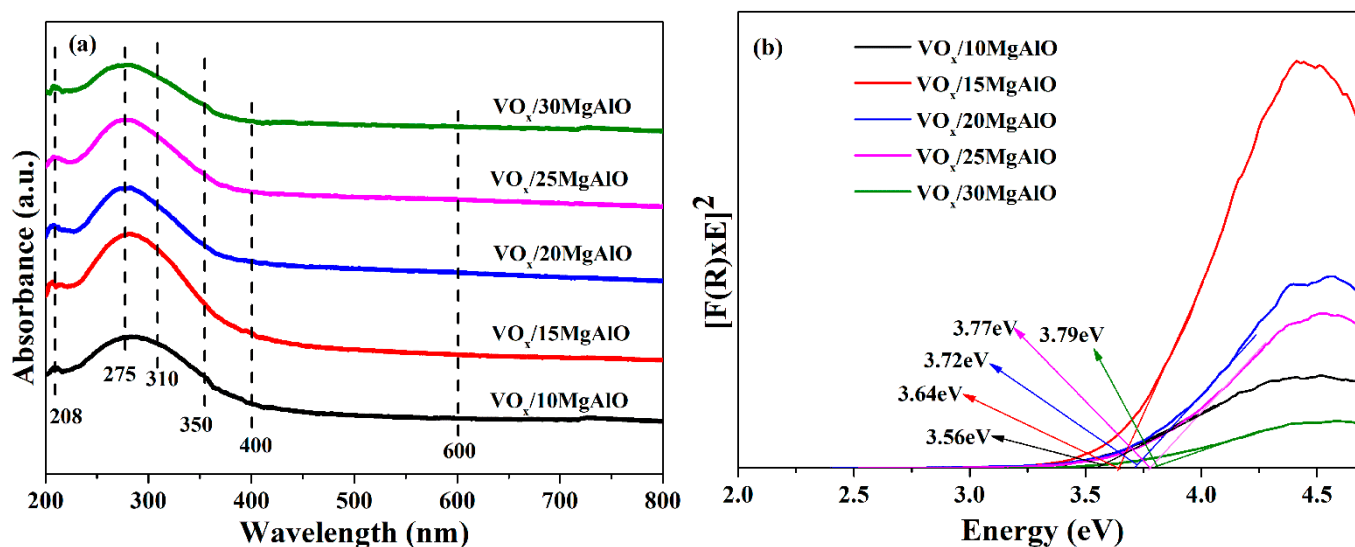


Figure 3. (a) Ultraviolet-visible diffuse reflectance (UV-Vis) spectra and (b) normalized UV-Vis spectra based on Kubelka–Munk for of the calcined catalyst $\text{VO}_x/m\text{MgAlO}$ ($m = 10, 15, 20, 25$ and 30).

The change of edge energy (E_g) corresponds to the change of polymerization degree of VO_x species on the catalyst surface [22]. As shown in Figure 3b, the E_g value slightly increases with increasing Mg content from 10% to 30%, further indicating that the polymerization degree of VO_x species gradually decreases and that more isolated and low-polymerized VO_x species are formed, which is consistent with the result of the Raman spectra above.

2.1.3. Surface Acidic Properties of Catalysts

Besides the aim to disperse VO_x species, another important aspect is the modification of Mg on the acidity of catalysts; therefore, the NH_3 temperature-programmed desorption (NH_3 -TPD) profiles of catalysts with different Mg content were used to analyze the acid sites of the catalysts, and the curves are drawn in Figure 4. Each curve can be fitted into three peaks, centered at ca. 160 °C (Peak I), 250 °C (Peak II) and 390 °C (Peak III), which are associated with the NH_3 desorption from the weak, medium and strong acid sites, respectively [26,42,43]. The peak area fractions and peak temperatures (T_{max}) related to the relative concentration and strength of acid sites are collected in Table 2.

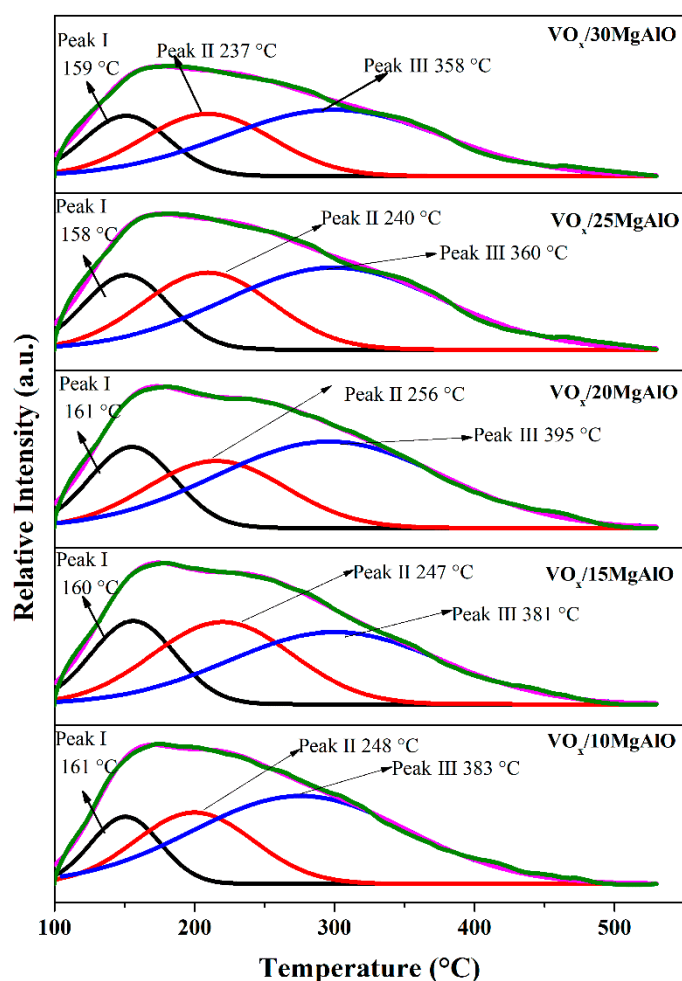


Figure 4. NH₃ temperature-programmed desorption (NH₃-TPD) profiles of the calcined catalyst VO_x/10MgAlO (m = 10, 15, 20, 25 and 30).

Table 2. The temperature and ratio of acid sites of VO_x/mMgAlO (m = 10, 15, 20, 25 and 30).

Catalysts	T _{max} (°C)			Peak Area Ratio (%)		
	Peak I	Peak II	Peak III	Peak I	Peak II	Peak III
VO _x /10MgAlO	159	237	358	25	50	25
VO _x /15MgAlO	158	240	363	21	62	17
VO _x /20MgAlO	161	256	395	23	66	11
VO _x /25MgAlO	160	247	381	25	68	7
VO _x /30MgAlO	161	248	383	27	65	8

It can be noted that there is no obvious difference in the concentration and strength of the weak acid sites among these catalysts, which suggests that the influence of Mg on the weak acidity can be ignored. However, the concentration of medium acid sites presents a rising trend, with increasing Mg content from 10% to 25%, and then falls back to a lower value than that of VO_x/20MgAlO, as the Mg content further increases to 30%. At the same time, an opposite trend can be found for the concentration change of strong acid sites with Mg content increasing. According to the result, it can be deduced that the introduced Mg species preferentially interact with strong acid sites on the Al₂O₃ support; therefore, the greater the Mg content is, the more the strong acid sites are neutralized and the larger the relative amount of the medium acid site that remains. Additionally, the strength of medium and strong acid sites can be enhanced by increasing the Mg content from 10% to 20%. This is related to the improving dispersion of VO_x species,

which is promoted by forming specific LDH derivatives as described above. Once the Mg content exceeds 20%, the acid strength drops to a constant level. Obviously, the coverage of excessive Mg species on the acid sites is an important reason to decrease the acidity of $\text{VO}_x/25\text{MgAlO}$ and $\text{VO}_x/30\text{MgAlO}$ [25]. Generally, the different surface acidity of catalysts can affect the isobutane dehydrogenation. The enhancement of medium acidity could facilitate dehydrogenation behavior by establishing a balance between the adsorption of light alkanes and the desorption of alkenes; accordingly, the side reactions and even coke formation can be inhibited, which favors prolonging the lifespan of catalysts [10,42–44].

2.1.4. Reducibility and Surface Chemical State of VO_x Species

The reduction behavior of the supported VO_x species was evaluated by temperature-programmed reduction (H_2 -TPR), and the profiles are displayed in Figure 5. As shown in Figure S2, no reduction peak can be found in the TPR profile of the bare support. This indicates the Al_2O_3 support cannot be reduced in the temperature range. All the catalysts present a single peak at around 550 °C, with a broad frontal peak. This must be related to the reduction of VO_x species with various V-O bands [22,26]. Usually, the reduction process of VO_x species is proposed from V^{5+} to V^{4+} and to V^{3+} [13–15]. With the increase of Mg content, the reduction peak temperature increases from 531 °C of $\text{VO}_x/10\text{MgAlO}$ to 535 °C of $\text{VO}_x/15\text{MgAlO}$ and to 555 °C of others; meanwhile, the VO_x polymerization degree presents a decreasing tendency, as illustrated by the Raman spectra above. It can be deduced that the higher reduction temperature suggests a stronger VO_x -support interaction and a better dispersion of VO_x species on the support. This must be related to the promoting role of reconstructed LDH intercalated with $[\text{V}_{10}\text{O}_{28}]^{6-}$ anions in the stability and separation of VO_x species [39]. Another reason for the poor reducibility for $\text{VO}_x/25\text{MgAlO}$ and $\text{VO}_x/30\text{MgAlO}$ can be attributed to the cover of excessive MgO . Although the strong VO_x -support interaction is beneficial to stabilizing active VO_x species, it can result in the loss of isobutene selectivity to some extent, as a consequence of decreasing the electron density of V-O-Al [10,26]. In order to deeply investigate the reduction behavior of catalysts, these TPR profiles are deconvoluted into three peaks; the detailed parameters, including peak temperature, peak area percentage, consumed hydrogen amount and average oxidation state (AOS_a) of VO_x , are summarized in Table S1. From low to high temperature, three peaks can be assigned to the reduction of isolated monomeric VO_x species (Peak I), oligomeric VO_x species (Peak II) and high polymeric VO_x species (Peak III), respectively [13–15,45]. The percentage of oligomeric VO_x species is more than twice that of isolated monomeric VO_x species, while the percentage of high polymeric VO_x species is so small that it can be ignored. This indicates that the VO_x species mainly belong to oligomeric and isolated states. Even $\text{VO}_x/25\text{MgAlO}$ presents the highest percentage of isolated monomeric VO_x species. This further proves the deduction drawn from the results of Raman and UV-Vis spectra above. Additionally, the AOS_a values of main oligomeric VO_x species show a slight increase with the increase of Mg content. The decreasing reducibility of VO_x species can be used to explain this phenomenon.

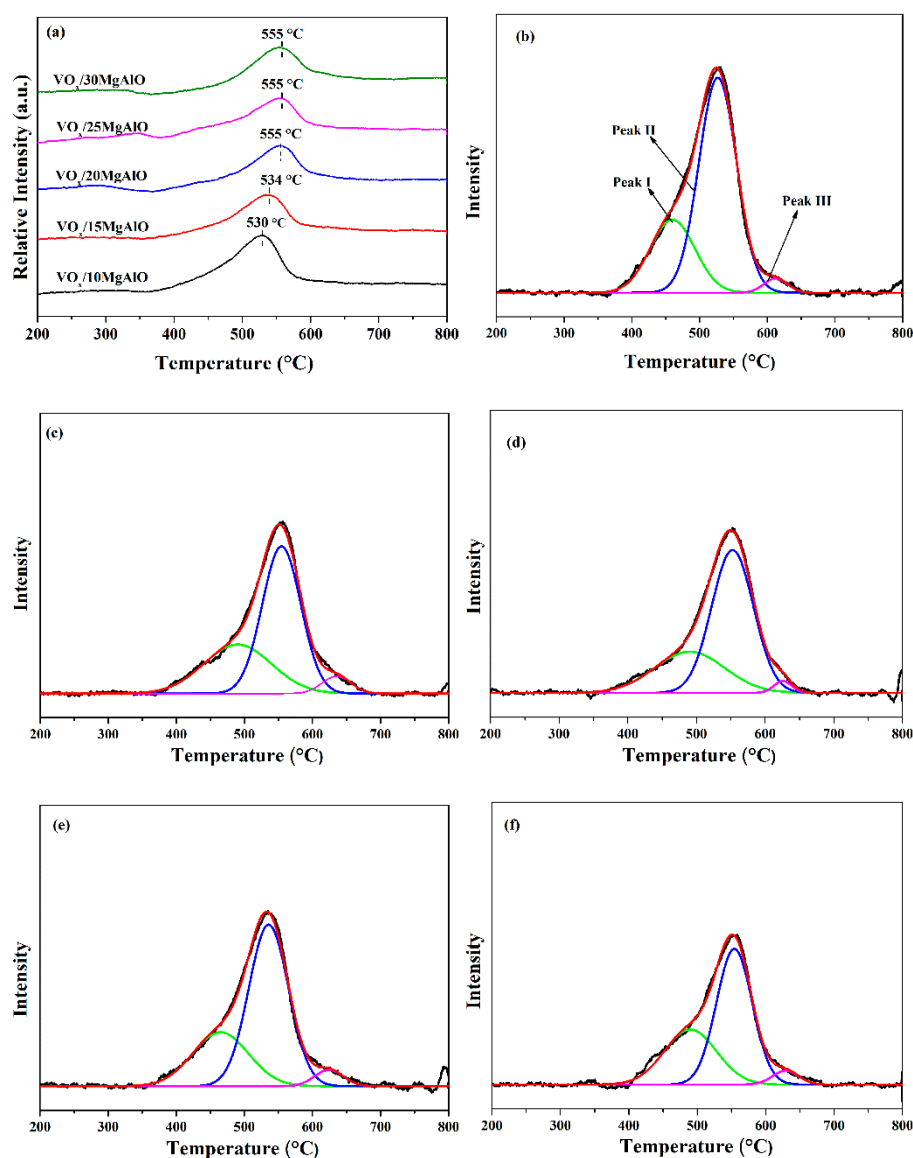


Figure 5. (a) Temperature-programmed reduction (H_2 -TPR) profiles for the calcined catalysts $VO_x/mMgAlO$ ($m = 10, 15, 20, 25$ and 30) and the corresponding deconvoluted Gaussian-shaped peaks of (b) $VO_x/10MgAlO$, (c) $VO_x/15MgAlO$, (d) $VO_x/20MgAlO$, (e) $VO_x/25MgAlO$, (f) $VO_x/30MgAlO$.

However, the low-valence VO_x species are considered to be the active sites [10,11,22]; therefore, the valence distribution and the average oxidation state (AOS_b) of surface VO_x species are further evaluated by X-ray photoelectron spectroscopy (XPS). All XPS spectra of the reduced catalysts are displayed in Figure 6, and the deconvolution results are summarized in Table 3. Only one broad peak can be found in the V $2p_{3/2}$ region, and the corresponding binding energy (BE) increases from 516.6 eV to 517.0 eV in the following order: $VO_x/10MgAlO-R < VO_x/15MgAlO-R < VO_x/20MgAlO-R \approx VO_x/25MgAlO-R \approx VO_x/30MgAlO-R$. This further proves the decrease of the VO_x species electron density and enhancement of VO_x -support interaction along with the Mg increasing to 20%, which is consistent with the H_2 -TPR result. Additionally, the original peak can be deconvoluted into three peaks related to V^{3+} , V^{4+} and V^{5+} ion [10,11,26]. It can be found that the AOS_b of VO_x species and the fraction of V^{5+} ion calculated by XPS deconvolution results exhibits a slightly rising tendency with increasing Mg content, which is also in agreement with the reducibility of catalysts analyzed by H_2 -TPR. This suggests that the fraction of low valence V ions, including V^{3+} and V^{4+} ions, tends to be reduced with increasing Mg content, especially for the V^{3+} ion. However, there is more

V^{4+} ion for $VO_x/15MgAlO-R$ and $VO_x/20MgAlO-R$ than the others. In the dehydrogenation process, the coke is more conducive to forming on V^{3+} sites than that on V^{4+} sites [35]. This suggests that the serious coking behavior is related to the relatively low AOS_b of VO_x species in catalysts, which can be tuned by changing the Mg content.

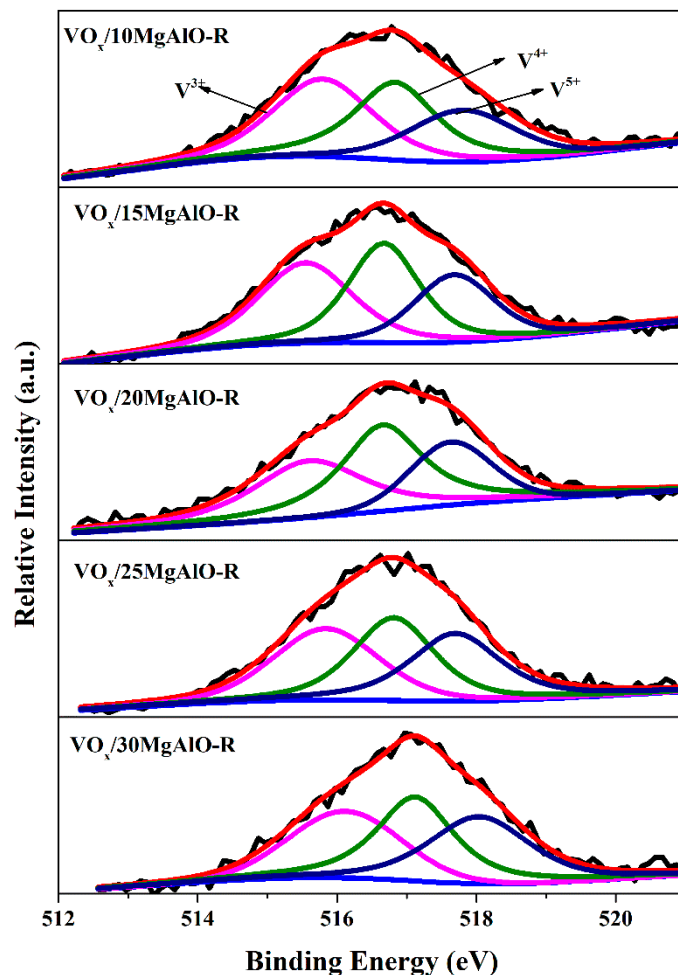


Figure 6. XPS of V $2p_{3/2}$ region of the reduced catalyst $VO_x/mMgAlO-R$ ($m = 10, 15, 20, 25$ and 30).

Table 3. The valence distribution and average oxidation state (AOS_b) of surface VO_x species determined by X-ray photoelectron spectroscopy (XPS).

Reduced Catalysts	V^{3+} (%)	V^{4+} (%)	V^{5+} (%)	AOS
$VO_x/10MgAlO-R$	39	36	25	3.86
$VO_x/15MgAlO-R$	37	37	26	3.89
$VO_x/20MgAlO-R$	35	37	28	3.93
$VO_x/25MgAlO-R$	34	34	32	3.98
$VO_x/30MgAlO-R$	31	36	33	4.03

2.2. Coking Behavior on the Used Catalysts

Carbon deposition usually occurs with the dehydrogenation process. The deposited carbon is one of the most important causes of catalyst deactivation. Therefore, it is necessary to evaluate the carbon deposition behavior on the catalysts by thermogravimetric analysis (TG) and XRD. As shown in Figure 7, the TG curves show significant mass loss at about $550\text{ }^\circ\text{C}$ for $VO_x/mMgAlO-R$ ($m = 10, 15, 20, 25$ and 30). With the increase of Mg content, the mass loss presents a sharp drop from 21% of $VO_x/10MgAlO-R$ to 18% of $VO_x/15MgAlO-R$ and to 13% $VO_x/20MgAlO-R$. Meanwhile, the mass loss for catalysts with high Mg content,

from 20–30%, is similar. Combined with the characteristic results of fresh catalysts, the coke accumulation is dependent on the amount of strong acid sites, the polymerization degree and the AOS of VO_x species. Certainly, the poor dehydrogenation activity as a consequence of covering VO_x species by excessive MgO also cannot be excluded as a reason for the lower amount of coke deposition of $\text{VO}_x/25\text{MgAlO-R}$ and $\text{VO}_x/30\text{MgAlO-R}$. It can be deduced that the excellent coking resistance of $\text{VO}_x/20\text{MgAlO-R}$ is a result of the relatively high concentration of strong acid sites, low polymerization degree of VO_x species and high AOS of surface VO_x species, which is close to 4+ state (see Table 3) [10,22,46]. Instead, heavy coke deposition occurs on $\text{VO}_x/10\text{MgAlO-R}$ and $\text{VO}_x/15\text{MgAlO-R}$, which could result in quick deactivation.

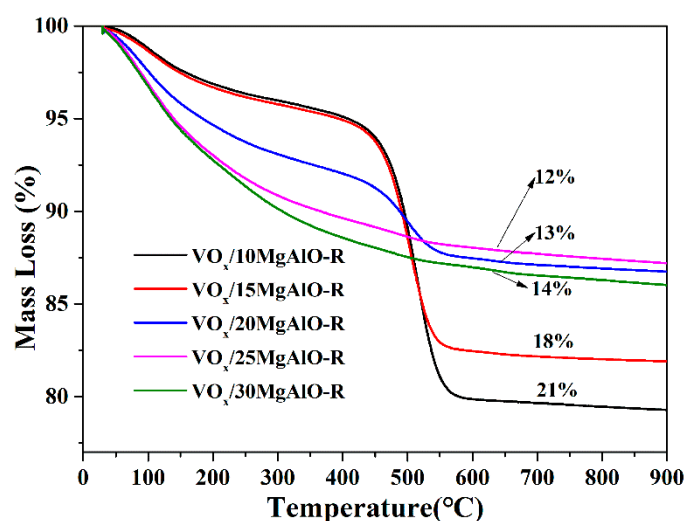


Figure 7. Thermogravimetric analysis (TG) profiles for the used catalyst $\text{VO}_x/m\text{MgAlO-R}$ ($m = 10, 15, 20, 25$ and 30) after reaction for 7.5 h.

The XRD patterns of the used catalysts $\text{VO}_x/m\text{MgAlO-R}$ ($m = 10, 15, 20, 25$ and 30) are shown in Figure 8. It can be seen that the samples still retain the peaks of MgO and $\gamma\text{-Al}_2\text{O}_3$ after a long reaction time, but there is no peak of carbonaceous species for all samples after the reaction, which means that the deposited coke is amorphous, thus making them easy to be regenerated in the next step.

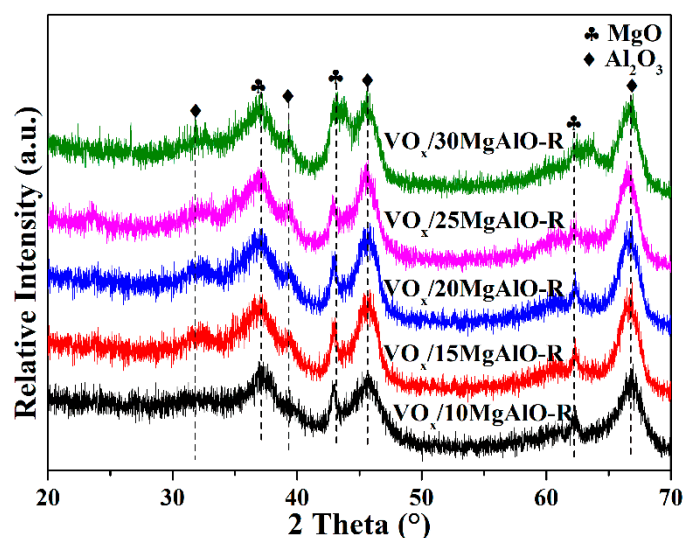


Figure 8. XRD patterns of the used catalyst $\text{VO}_x/m\text{MgAlO-R}$ ($m = 10, 15, 20, 25$ and 30) after reaction for 7.5 h.

2.3. Catalytic Performance

The curves with the time on stream of isobutane dehydrogenation on the reduced catalyst $\text{VO}_x/\text{mMgAlO-R}$ ($m = 10, 15, 20, 25, 30$) are displayed in Figure 9. The isobutane conversions follow a decreasing trend from $\text{VO}_x/20\text{MgAlO-R}$ to $\text{VO}_x/15\text{MgAlO-R}$ to $\text{VO}_x/10\text{MgAlO-R}$ to $\text{VO}_x/25\text{MgAlO-R}$ and to $\text{VO}_x/30\text{MgAlO-R}$ in most reaction periods. The enhancement of isobutane conversion from $\text{VO}_x/10\text{MgAlO-R}$ to $\text{VO}_x/15\text{MgAlO-R}$ and to $\text{VO}_x/20\text{MgAlO-R}$ is related to the decreasing polymerization degree of the VO_x species, elevating the concentration and strength of medium acid sites and increasing AOS close to a 4+ state. However, the poor dehydrogenation activity of $\text{VO}_x/25\text{MgAlO-R}$ and $\text{VO}_x/30\text{MgAlO-R}$ mainly arises from the partial surface VO_x covered by excessive MgO , because the addition of excessive Mg can lead to the overflow of MgO [25]. Additionally, all catalysts present a decreasing activity with time on stream in the reaction, and the decline degree is correlated well with the amount of coke deposition. The dramatic activity loss of $\text{VO}_x/10\text{MgAlO-R}$ and $\text{VO}_x/15\text{MgAlO-R}$ is likely due to the severe coke formation during the whole reaction [22]. The stable dehydrogenation behavior of the others is related to their strong VO_x -support interaction, which can prevent the aggregation of VO_x species. In particular, the catalyst $\text{VO}_x/20\text{MgAlO-R}$ shows maximum activity, but its isobutane conversion only shows a slight decrease from the initial 56% to 43% after reaction of 7.5 h.

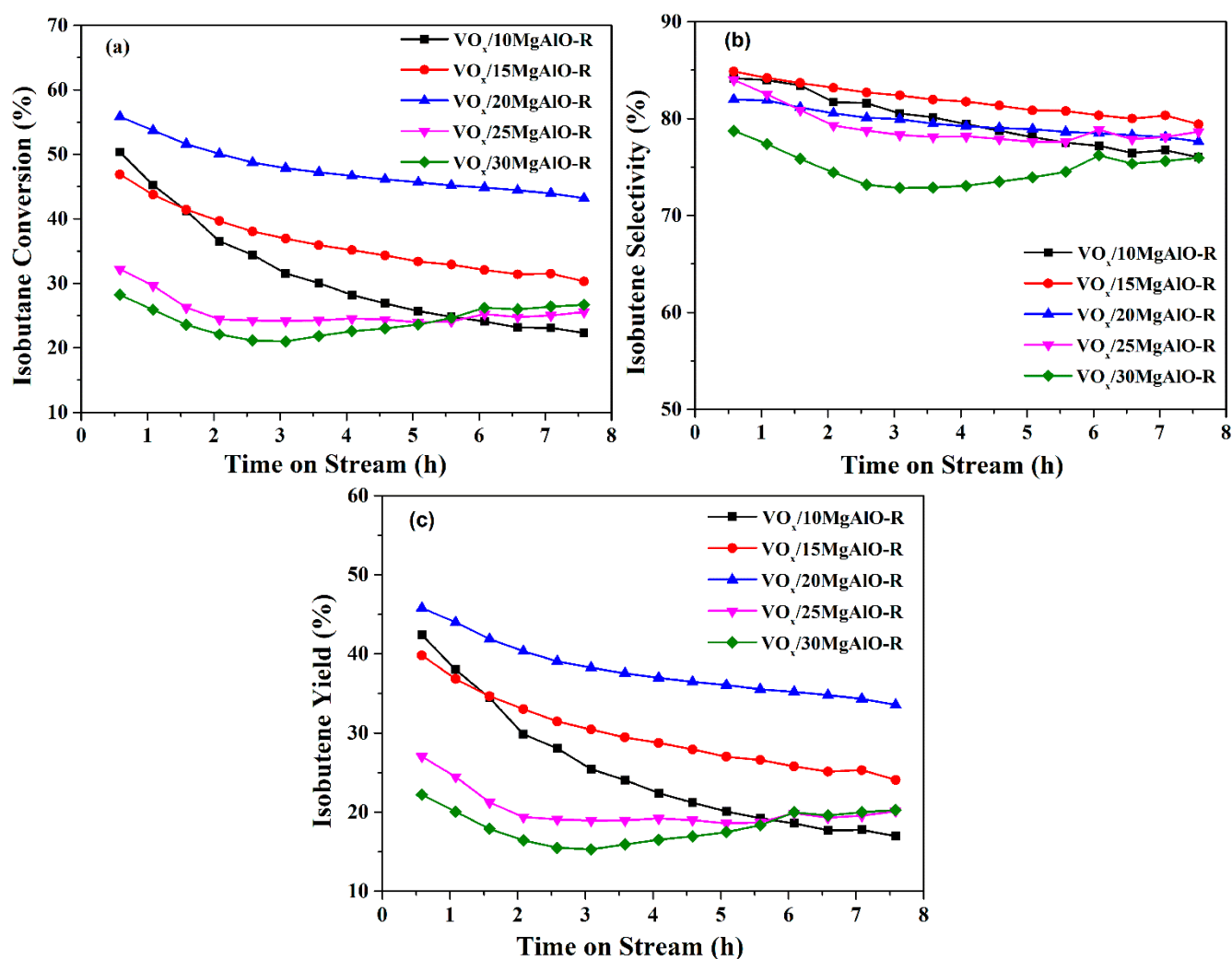


Figure 9. (a) Isobutane conversion, (b) isobutene selectivity and (c) isobutene yield vs. reaction time for the reduced catalyst $\text{VO}_x/\text{mMgAlO-R}$ ($m = 10, 15, 20, 25$ and 30) (dehydrogenation conditions: $T = 600\text{ }^\circ\text{C}$, $\text{WHSV} = 3\text{ h}^{-1}$, $i\text{C}_4\text{H}_{10}:\text{H}_2 = 1:1$ (molar ratio), $m_{\text{cat}} = 0.5\text{ g}$).

As for the isobutene selectivity and yield, the trends with reaction time are similar to those of isobutane conversion for all catalysts, except the isobutene selectivity of VO_x/20MgAlO-R, which is slightly lower than that of VO_x/15MgAlO-R but not less than 72%. The result agrees well with the deduction from H₂-TPR. That is to say, the most likely reason for the lower isobutene selectivity of VO_x/20MgAlO-R is related to the lower electron density of V-O-Al arising from the stronger interaction between the VO_x and support, which makes isobutene more difficult to desorb from the surface of VO_x/20MgAlO-R, thus resulting in the side reactions and further low selectivity. Although there is slight loss of isobutene selectivity, the stability of VO_x/20MgAlO-R is effectively improved, and the superior isobutene yield, more than 33%, is achieved as expected.

3. Materials and Methods

3.1. Materials

The required materials include MgCl₂·6H₂O (98.0% purity, Tianjin Kermel Chemical Reagents Co., Ltd., Tianjin, China), urea (99.0% purity, DAMAO Chemical Reagents Co., Ltd., Tianjin, China), γ-Al₂O₃ (99.9% purity, Aladdin Reagent Co., Ltd., Shanghai, China), NH₄VO₃ (99.0% purity, Shanghai Meryer Chemical Technology Co., Ltd., Shanghai, China) and oxalic acid (99.0% purity, Shanghai Meryer Chemical Technology Co., Ltd., Shanghai, China).

3.2. Composite Oxide Support Preparation

The MgAl composite oxide support precursors with different Mg content were prepared by the hydrothermal method as described in our previous work [29]. First, MgCl₂·6H₂O and urea were dissolved in 65 mL deionized water with Mg/urea of 1/4 under vigorous stirring at room temperature. Then, 1.5 g γ-Al₂O₃ powder was added into the mixture solution. After fully stirring, the mixture was transferred into a 100 mL Teflon autoclave and heated at 120 °C for 20 h. Then, the composite precursor was obtained by filtering, washing and drying the mixture at 120 °C for 12 h, and it was marked as mMgAlO-P (m = 10, 15, 20, 25 and 30), where “m” is the theoretical weight percentage of MgO relative to γ-Al₂O₃. After calcining the precursor at 550 °C for 4 h, the corresponding γ-Al₂O₃-supported composite support was obtained and denoted as mMgAlO.

3.3. Catalyst Preparation

The composite supports mMgAlO-supported VO_x catalysts (VO_x/mMgAlO) with a V loading amount of 7 wt% were prepared by the traditional incipient impregnation method. First, the as-synthesized supports mMgAlO were impregnated with an aqueous solution containing NH₄VO₃ and oxalic acid, with the molar ratio of 1:2. The wet solids were aged in air at room temperature for 12 h, dried at 120 °C overnight, and finally calcined in a muffle furnace at 550 °C for 4 h with a heating rate of 2 °C·min⁻¹; the corresponding precursors were designated as VO_x/mMgAlO. Before reaction, these calcined samples were subjected to a high temperature pre-reduction treatment in 5 vol% H₂/N₂ (30 mL·min⁻¹) at 600 °C for 2 h, and the products were labeled as reduced catalysts VO_x/mMgAlO-R.

3.4. Catalyst Characterization

X-ray diffraction (XRD) characterization was carried out on D-Foucas (Bruker, Karlsruhe, Germany) equipped with a Cu Kα radiation (λ = 0.15418 nm), and the spectral scanning angle and scanning speed were 10–90° and 8°/min, respectively. A low-temperature N₂ adsorption–desorption test was performed on an automated analyzer (QUA211007, Quantachrome, Boynton, FL, USA). Raman spectra were measured at ambient conditions by a DXR Raman spectrometer (Thermo Fisher Scientific, Waltham, MA, USA) with an excitation wavelength of 532 nm. Ultraviolet-visible diffuse reflectance (UV-Vis) spectra (200–800 nm) were acquired on a Shimadzu UV-3600 spectrophotometer (Kyoto, Japan) in the region of 200–800 nm, Normalized UV-Vis spectra were drawn according to the Kubelka-Munk equation: $F(R) = (1 - R)^2 / 2R$, where R is reflectivity. A temperature-programmed reduction (H₂-TPR) experiment was carried out on automatic multipurpose adsorption

apparatus (tp5080 XQINSTRUMENT Co., Ltd., Tianjin, China). The NH₃ temperature-programmed desorption (NH₃-TPD) measurements were taken using a Micromeritics AutoChem II 2920 apparatus (Micromeritics, Norcross, GA, USA). The X-ray photoelectron spectroscopy (XPS) measurement was carried out using a Thermo ESCALAB 250Xi (US) (Thermo Fisher Scientific, Waltham, MA, USA), using Al K α radiation and a C1s level with a binding energy (BE) of 284.8 eV as an internal reference to obtain information on the chemical composition and chemical states of the elements located on the surface of the reduced catalysts. The coking behavior of the used catalysts was analyzed by thermogravimetric analysis (TG, HITACHI STA7300, HITACHI, Tokyo, Japan), with a heating rate of 10 °C·min⁻¹ from room temperature to 900 °C in air.

3.5. Catalytic Performance Test

The isobutane dehydrogenation reaction was carried out in a fixed bed reactor at 600 °C and atmospheric pressure; the inner diameter of the reaction tube was 8 mm, the amount of catalyst was 0.5 g (40–60 mesh). The reduction pretreatment was carried out in an atmosphere of 5% H₂ and 95% N₂. After that, the isobutane and hydrogen were mixed into the reaction tube at a molar ratio of 1:1. The weight hourly space velocity (WHSV) of isobutane was 3 h⁻¹, and the concentrations of all hydrocarbons involving C₄H₁₀, C₄H₈, C₃H₈, C₃H₆, C₂H₆, C₂H₄ and CH₄, were analyzed by an online gas chromatograph (GC) equipped with a flame ionization detector (FID). The carbon balance ranged between 96% and 102%, which was evaluated by comparing the number of moles of carbon in the outlet gases to the number of moles of carbon in the inlet C₄H₁₀ gas and calibrating by taking into consideration the coke amount determined by the TG measurement. The isobutane conversion, isobutene selectivity and yield were calculated as follows:

$$iC_4H_{10} \text{ Conversion} (\%) = \frac{iC_4H_{10} \text{ in} - iC_4H_{10} \text{ out}}{iC_4H_{10} \text{ in}} \times 100 \quad (1)$$

$$iC_4H_8 \text{ Selectivity} (\%) = \frac{iC_4H_8 \text{ out}}{iC_4H_{10} \text{ in} - iC_4H_{10} \text{ out}} \times 100 \quad (2)$$

$$iC_4H_8 \text{ Yield} (\%) = \text{Conversion} \times \text{Selectivity} \times 100 \quad (3)$$

4. Conclusions

The composite oxide-supported VO_x-based catalysts VO_x/mMgAlO-R (m = 10, 15, 20, 25 and 30) were successfully prepared and applied in the nonoxidative dehydrogenation of isobutane to isobutene. The composite oxide supports can be obtained by calcining in-situ synthesized MgAl-LDH/Al₂O₃. The catalytic performance strongly depends on the Mg content. The correlation between structure and catalytic performance reveals that the appropriate addition of Mg can help the formation of the reconstructed brucite-like lattice-confined VO_x species and abundant porous MgO, which facilitates dispersing and stabilizing the VO_x species by strongly interacting with the support, and thus promotes the formation of more isolated and low-polymerized VO_x species and a higher proportion of V⁴⁺ ions. These factors lead the catalyst VO_x/20MgAlO-R to exhibit superior activity and stability and excellent coke resistance, without significantly impairing isobutene selectivity. Additionally, the increase of Mg content could increase the consumption of the strong acid sites and enhance the strength and concentration of medium acid sites of the Al₂O₃ surface, thus resisting coke formation and improving dehydrogenation performance. The excess MgO formation could cover the surface of VO_x species and result in the dramatic loss in activity for VO_x/25MgAlO-R and VO_x/30MgAlO-R.

Supplementary Materials: The following supporting information can be downloaded at: <https://www.mdpi.com/article/10.3390/catal12040382/s1>, Figure S1: Low temperature N₂ adsorption-desorption isotherms (a) and pore size distribution curves (b) of the calcined catalysts VO_x/mMgAlO (m = 10, 15, 20, 25, 30); Figure S2: Temperature-programmed reduction (H₂-TPR) profiles for the bare support. Table S1: TPR data of the calcined catalysts VO_x/mMgAlO (m = 10, 15, 20, 25, 30).

Author Contributions: Conceptualization, F.L.; methodology, F.L. and M.H.; formal analysis, F.L. and X.L.; Investigation, F.L., Y.W. and X.Z.; resources, L.Z.; writing—original draft preparation, F.L.; writing—review and editing, Y.X. and L.Z.; supervision, L.Z.; project administration, L.Z.; funding acquisition, L.Z. All authors have read and agreed to the published version of the manuscript.

Funding: This research was funded by the National Natural Science Foundation of China (21776214).

Data Availability Statement: Data are contained within the article.

Acknowledgments: The authors gratefully thank the State Key Laboratory of Chemical Resource Engineering, Beijing University of Chemical Technology, China.

Conflicts of Interest: The authors declare no conflict of interest.

References

1. Sattler, J.J.; Ruiz-Martinez, J.; Santillan-Jimenez, E.; Weckhuysen, B.M. Catalytic dehydrogenation of light alkanes on metals and metal oxides. *Chem. Rev.* **2014**, *114*, 10613–10653. [[CrossRef](#)] [[PubMed](#)]
2. Zhu, G.L.; Li, P.H.; Zhao, F.; Song, H.L.; Xia, C.G. Selective aromatization of biomass derived diisobutylene to p-xylene over supported non-noble metal catalysts. *Catal. Today* **2016**, *276*, 105–111. [[CrossRef](#)]
3. Xie, Y.; Luo, R.; Sun, G.; Chen, S.; Zhao, Z.J.; Mu, R.; Gong, J. Facilitating the reduction of V-O bonds on VO_x/ZrO₂ catalysts for non-oxidative propane dehydrogenation. *Chem. Sci.* **2020**, *11*, 3845–3851. [[CrossRef](#)] [[PubMed](#)]
4. Zhu, Q.; Zhang, H.; Zhang, S.; Wang, G.; Zhu, X.; Li, C. Dehydrogenation of isobutane over a Ni-P/SiO₂ catalyst: Effect of P addition. *Ind. Eng. Chem. Res.* **2019**, *58*, 7834–7843. [[CrossRef](#)]
5. Chen, C.; Sun, M.L.; Hu, Z.P.; Ren, J.T.; Zhang, S.M.; Yuan, Z.Y. New insight into the enhanced catalytic performance of ZnPt/HZSM-5 catalysts for direct dehydrogenation of propane to propylene. *Catal. Sci. Technol.* **2019**, *9*, 1979–1988. [[CrossRef](#)]
6. Yang, Z.; Li, H.; Zhou, H.; Wang, L.; Wang, L.; Zhu, Q.; Xiao, J.; Meng, X.; Chen, J.; Xiao, F.S. Coking-resistant iron catalyst in ethane dehydrogenation achieved through siliceous zeolite modulation. *J. Am. Chem. Soc.* **2020**, *142*, 16429–16436. [[CrossRef](#)]
7. Chen, C.; Zhang, S.M.; Wang, Z.; Yuan, Z.Y. Ultrasmall Co confined in the silanols of dealuminated beta zeolite: A highly active and selective catalyst for direct dehydrogenation of propane to propylene. *J. Catal.* **2020**, *383*, 77–87. [[CrossRef](#)]
8. Liu, G.; Zeng, L.; Zhao, Z.J.; Tian, H.; Wu, T.F.; Gong, J.L. Platinum-modified ZnO/Al₂O₃ for propane dehydrogenation: Minimized platinum usage and improved catalytic stability. *ACS Catal.* **2016**, *6*, 2158–2162. [[CrossRef](#)]
9. Sokolov, S.; Stoyanova, M.; Rodemerck, U.; Linke, D.; Kondratenko, E.V. Comparative study of propane dehydrogenation over V-, Cr-, and Pt-based catalysts: Time on-stream behavior and origins of deactivation. *J. Catal.* **2012**, *293*, 67–75. [[CrossRef](#)]
10. Gu, Y.; Liu, H.J.; Yang, M.M.; Ma, Z.P.; Zhao, L.M.; Xing, W.; Wu, P.P.; Liu, X.M.; Mintova, E.L.N.; Bai, P.; et al. Highly stable phosphine modified VO_x/Al₂O₃ catalyst in propane dehydrogenation. *Appl. Catal.* **2020**, *274*, 119809. [[CrossRef](#)]
11. Bai, P.; Ma, Z.; Li, T.; Tian, Y.; Zhang, Z.; Zhong, Z.; Xing, W.; Wu, P.; Liu, X.; Yan, Z. Relationship between surface chemistry and catalytic performance of mesoporous γ -Al₂O₃ supported VO_x catalyst in catalytic dehydrogenation of propane. *ACS Appl. Mater. Interfaces* **2016**, *8*, 25979–25990. [[CrossRef](#)] [[PubMed](#)]
12. Kong, N.; Fan, X.; Liu, F.; Wang, L.; Lin, H.; Li, Y.; Lee, S.T. Single vanadium atoms anchored on graphitic carbon nitride as a high-performance catalyst for non-oxidative propane dehydrogenation. *ACS Nano* **2020**, *14*, 5772–5779. [[CrossRef](#)] [[PubMed](#)]
13. Dasireddy, V.D.B.C.; Singh, S.; Friedrich, H.B. Effect of the Support on the oxidation of heptane using vanadium supported on alkaline earth metal hydroxyapatites. *Catal. Lett.* **2014**, *145*, 668–678. [[CrossRef](#)]
14. Dasireddy, V.D.B.C.; Friedrich, H.B.; Singh, S. Studies towards a mechanistic insight into the activation of n-octane using vanadium supported on alkaline earth metal hydroxyapatites. *Appl. Catal. A Gen.* **2013**, *467*, 142–153. [[CrossRef](#)]
15. Dasireddy, V.D.B.C.; Singh, S.; Friedrich, H.B. Vanadium oxide supported on non-stoichiometric strontium hydroxyapatite catalysts for the oxidative dehydrogenation of n-octane. *J. Mol. Catal. A Chem.* **2014**, *395*, 398–408. [[CrossRef](#)]
16. Tian, Y.P.; Liu, X.M.; Zhan, W.L.; Cheng, S.X.; Zhang, L.L.; Yan, Z.F. Elucidation of active species and reaction mechanism of sulfide V-K/Al₂O₃ catalyst for isobutane dehydrogenation. *Appl. Surf. Sci.* **2021**, *569*, 5772–5779. [[CrossRef](#)]
17. Tian, Y.P.; Liu, X.M.; Mintova, S.; Zhang, L.L.; Pan, Y.Y.; Rives, A.; Liu, Y.A.; Wei, L.; Yan, Z.F. Isobutane dehydrogenation over high-performanced sulfide V-K/ γ -Al₂O₃ catalyst: Modulation of vanadium species and intrinsic effect of potassium. *J. Colloid Interface Sci.* **2021**, *600*, 440–448. [[CrossRef](#)]
18. Hu, P.; Lang, W.Z.; Yan, X.; Chu, L.F.; Guo, Y.J. Influence of gelation and calcination temperature on the structure-performance of porous VO_x-SiO₂ solids in non-oxidative propane dehydrogenation. *J. Catal.* **2018**, *358*, 108–117. [[CrossRef](#)]
19. Chen, C.; Sun, M.; Hu, Z.; Liu, Y.; Zhang, S.; Yuan, Z.Y. Nature of active phase of VO catalysts supported on SiBeta for direct dehydrogenation of propane to propylene. *Chin. J. Catal.* **2020**, *41*, 276–285. [[CrossRef](#)]
20. Rodemerck, U.; Stoyanova, M.; Kondratenko, E.V.; Linke, D. Influence of the kind of VO_x structures in VO_x/MCM-41 on activity, selectivity and stability in dehydrogenation of propane and isobutane. *J. Catal.* **2017**, *352*, 256–263. [[CrossRef](#)]
21. Kaichev, V.V.; Chesalov, Y.A.; Saraev, A.A.; Tsapina, A.M. A Mechanistic Study of Dehydrogenation of Propane over Vanadia-Titania Catalysts. *J. Phys. Chem. C* **2019**, *123*, 19668–19680. [[CrossRef](#)]
22. Liu, G.; Zhao, Z.J.; Wu, T.F.; Zeng, L.; Gong, J.L. Nature of the active sites of VO_x/Al₂O₃ catalysts for propane dehydrogenation. *ACS Catal.* **2016**, *6*, 5207–5214. [[CrossRef](#)]

23. Rodemerck, U.; Sokolov, S.; Stoyanova, M.; Bentrup, U.; Linke, D.; Kondratenko, E.V. Influence of support and kind of VO species on isobutene selectivity and coke deposition in non-oxidative dehydrogenation of isobutane. *J. Catal.* **2016**, *338*, 174–183. [[CrossRef](#)]
24. Wang, X.S.; Zhou, G.L.; Chen, Z.W.; Li, Q.; Zhou, H.J.; Xu, C.M. Enhancing the vanadium dispersion on V-MCM-41 by boron modification for efficient iso-butane dehydrogenation. *Appl. Catal. A* **2018**, *555*, 171–177. [[CrossRef](#)]
25. Wu, T.F.; Liu, G.; Zeng, L.; Sun, G.D.; Chen, S.; Mu, R.T.; Gbonfoun, S.A.; Zhao, Z.J.; Gong, J.L. Structure and catalytic consequence of Mg-modified VO_x/Al₂O₃ catalysts for propane dehydrogenation. *AIChE J.* **2017**, *63*, 4911–4919. [[CrossRef](#)]
26. Shan, Y.L.; Zhao, W.T.; Zhao, S.L.; Wang, X.X.; Sun, H.L.; Yu, W.L.; Ding, J.W.; Feng, X.; Chen, D. Effects of alumina phases on the structure and performance of VO_x/Al₂O₃ catalysts in non-oxidative propane dehydrogenation. *Mol. Catal.* **2021**, *504*, 111466. [[CrossRef](#)]
27. Wu, Z.; Stair, P. UV Raman spectroscopic studies of V/θ-Al₂O₃ catalysts in butane dehydrogenation. *J. Catal.* **2006**, *237*, 220–229. [[CrossRef](#)]
28. Zhang, M.; Song, Z.; Guo, M.Q.; Li, X.X.; Lin, Y.J.; Zhang, L.H. Effect of reduction atmosphere on structure and catalytic performance of PtIn/Mg(Al)O/ZnO for propane dehydrogenation. *Catalysts* **2020**, *10*, 485. [[CrossRef](#)]
29. Li, J.X.; Zhang, M.; Song, Z.; Liu, S.; Wang, J.M.; Zhang, L.H. Hierarchical PtIn/Mg(Al)O derived from reconstructed PtIn-hydroxalcalite-like compounds for highly efficient propane dehydrogenation. *Catalysts* **2019**, *9*, 767. [[CrossRef](#)]
30. Xia, K.; Lang, W.Z.; Li, P.P.; Long, L.L.; Yan, X.; Guo, Y.J. The influences of Mg/Al molar ratio on the properties of PtIn/Mg(Al)O-x catalysts for propane dehydrogenation reaction. *Chem. Eng. J.* **2016**, *284*, 1068–1079. [[CrossRef](#)]
31. Zhu, Y.R.; An, Z.; Song, H.Y.; Xiang, X.; Yang, W.J.; He, J. Lattice-confined Sn (IV/II) stabilizing raft-like Pt clusters: High selectivity and durability in propane dehydrogenation. *ACS Catal.* **2017**, *7*, 6973–6978. [[CrossRef](#)]
32. Aboelfetoh, E.F.; Pietschnig, R. Preparation, characterization and catalytic activity of MgO/SiO₂ supported vanadium oxide based catalysts. *Catal. Lett.* **2013**, *144*, 97–103. [[CrossRef](#)]
33. Tan, C.; Guo, Y.F.; Sun, J.; Li, W.L.; Zhang, J.B.; Zhao, C.W.; Lu, P. Structurally improved MgO adsorbents derived from magnesium oxalate precursor for enhanced CO₂ capture. *Fuel* **2020**, *278*, 118379. [[CrossRef](#)]
34. Ding, Y.D.; Song, G.; Zhu, X.; Chen, R.; Liao, Q. Synthesizing MgO with a high specific surface for carbon dioxide adsorption. *RSC Adv.* **2015**, *5*, 30929–30935. [[CrossRef](#)]
35. Zhang, L.; Zhu, W.; Zhang, H.; Bi, S.; Zhang, Q. Hydrothermal–thermal conversion synthesis of hierarchical porous MgO microrods as efficient adsorbents for lead(II) and chromium(VI) removal. *RSC Adv.* **2014**, *4*, 30542–30550. [[CrossRef](#)]
36. Zeng, S.B.; Xu, X.L.; Wang, S.K.; Gong, Q.K.; Liu, R.J.; Yu, Y. Sand flower layered double hydroxides synthesized by co-precipitation for CO₂ capture: Morphology evolution mechanism, agitation effect and stability. *Mater. Chem. Phys.* **2013**, *140*, 159–167. [[CrossRef](#)]
37. Jin, X.; Wang, R.; Zhou, Y.; Lai, J.; Li, J.; Pei, G.; Chen, S.; Wang, X.; Xiang, J.; Zhu, Z.; et al. A comprehensive experimental and first-principles study on magnesium–vanadium oxides. *J. Alloys Compd.* **2022**, *896*, 162862. [[CrossRef](#)]
38. Ono, T.; Ogata, N.; Numata, H.; Miyaryo, Y. A study of active sites for alkene and alkane oxidation over Mo and V mixed oxide catalysts using ¹⁸O tracer and Raman spectroscopy. *Top. Catal.* **2001**, *15*, 2–4. [[CrossRef](#)]
39. Miao, C.L.; Hui, T.L.; Liu, Y.N.; Feng, J.T.; Li, D.Q. Pd/MgAl-LDH nanocatalyst with vacancy-rich sandwich structure: Insight into interfacial effect for selective hydrogenation. *J. Catal.* **2019**, *370*, 107–117. [[CrossRef](#)]
40. Kondratenko, E.V.; Cherian, M.; Baerns, M. Oxidative dehydrogenation of propane over differently structured vanadia-based catalysts in the presence of O₂ and N₂O. *Catal. Today* **2006**, *112*, 60–63. [[CrossRef](#)]
41. Rajan, N.P.; Rao, G.S.; Putrakumar, B.; Chary, K.V.R. Vapour phase dehydration of glycerol to acrolein over vanadium phosphorous oxide (VPO) catalyst. *RSC Adv.* **2014**, *4*, 53419–53428. [[CrossRef](#)]
42. Chen, X.; Ge, M.; Li, Y.; Liu, Y.; Wang, J.; Zhang, L. Fabrication of highly dispersed Pt-based catalysts on γ-Al₂O₃ supported perovskite nano islands: High durability and tolerance to coke deposition in propane dehydrogenation. *Appl. Surf. Sci.* **2019**, *490*, 611–621. [[CrossRef](#)]
43. Wang, J.M.; Song, Z.; Han, M.X.; Li, X.X.; Zhang, L.H. Molybdenum-based catalysts supported on alumina for direct dehydrogenation of isobutane. *Mol. Catal.* **2021**, *511*, 111746. [[CrossRef](#)]
44. Li, Y.Y.; Ge, M.; Wang, J.M.; Guo, M.Q.; Liu, F.J.; Han, M.X.; Xu, Y.H.; Zhang, L.H. Dehydrogenation of isobutane to isobutene over a Pt-Cu bimetallic catalyst in the presence of LaAlO₃ perovskite. *Chin. J. Chem. Eng.* **2021**, *32*, 203–211. [[CrossRef](#)]
45. Tian, Y.P.; Bai, P.; Liu, S.M.; Liu, X.-M.; Yan, Z.F. VO_x-K₂O/γ-Al₂O₃ catalyst for nonoxidative dehydrogenation of isobutane. *Fuel Process. Technol.* **2016**, *151*, 31–39. [[CrossRef](#)]
46. Zhao, Z.J.; Wu, T.; Xiong, C.; Sun, G.; Mu, R.; Zeng, L.; Gong, J. Hydroxyl-mediated non-oxidative propane dehydrogenation over VO_x/γ-Al₂O₃ catalysts with improved stability. *Angew. Chem. Int. Ed. Engl.* **2018**, *57*, 6791–6795. [[CrossRef](#)]